



Shahid Chamran
University of Ahvaz

Journal of Applied and Computational Mechanics



Research Paper

Distributed-parameter Dynamic Modeling and Bifurcation Analysis of a Trapezoidal Piezomagnetoelastic Energy Harvester

Heshmatallah Mohammad Khanlo¹, Reza Dehghani²

¹ Department of Aerospace Engineering, Shahid Sattari Aeronautical University of Science and Technology, Tehran, 13846-63113, Iran, Email: H_khanloo@ssau.ac.ir

² Department of Design and Manufacturing Engineering, Graduate University of Advanced Technology, Kerman, 76311-33131, Iran, Email: R.dehghani@kgut.ac.ir

Received August 26 2019; Revised December 06 2019; Accepted for publication December 06 2019.

Corresponding author: R. Dehghani (R.dehghani@kgut.ac.ir)

© 2022 Published by Shahid Chamran University of Ahvaz

Abstract. In this paper, the effect of the bimorph profile on the nonlinear dynamic behavior and performance of a vibratory piezomagnetoelastic energy harvester is investigated. The proposed model is composed of upper and lower piezoelectric layers on a trapezoidal cantilever beam with one attached tip magnet as well as two external magnets. The magnetic field of two external magnets generates magnetic forces and moment on the tip magnet. The bimorph structure is considered as a distributed-parameter system, and the external forces are obtained by analyzing the magnetic field of the external magnets. Equations of motion are obtained using electromagnetic Lagrange equations based on the generalized Hamilton principle and the Euler-Bernoulli beam theory. The proposed model for the bimorph and magnetic forces is validated by previously published experimental results. In order to compare the nonlinear behavior of the rectangular and trapezoidal beam profiles, the bifurcation diagrams are depicted for various control parameters such as the separation distances of the magnets, beam root width, and beam tip width. Verification of the bifurcation diagrams is performed by the phase plane portraits and Poincare maps. Also, the harvested power level is compared for different profiles of the bimorph. Moreover, the simultaneous effects of exciting frequency and bifurcation parameters on the system performance are investigated by the waterfall diagrams. The obtained results show that the trapezoidal beam profile with a lower tip width has higher performance than the rectangular beam. In trapezoidal beam profiles, the subharmonic and chaotic motions have relatively higher output powers than periodic motions.

Keywords: Energy harvesting; Piezoelectric layers; Trapezoidal beam; Magnetic field; Chaotic.

1. Introduction

In recent years, the vibratory energy harvesting systems due to their various applications have more attractive research areas for many researchers than before. Vibration sources are generally more accessible in many locations. They can provide high energy density per unit device volume than other sources. The aim is to provide energy for various devices using the vibrational energy available in the environment. There are mainly three different methods that are most popular and extensively studied in researches based on piezoelectric, electromagnetic, and electrostatic transductions [1]. In these types of energy harvesters, the piezoelectric transducers are used to transform the mechanical vibrations into electrical energy. Most piezoelectric energy harvesters are in the form of cantilevered unimorph or bimorph beams configurations. The harvester beam can be located on a main structure, and the vibratory motions induced in piezoelectric layers result in an output voltage across their electrodes.

One of the important issues in this field is the appropriate mathematical model of the vibratory energy harvesting systems, and it should be included all of the physical behavior characteristics of the system. This makes the simulation results more reliable. In two recent decades, many researchers have tried to improve the early mathematical lumped models [2, 3] to relatively real physical models such as the Rayleigh-Ritz model [4, 5], the finite element model [6-8] and the distributed parameter model [9-12]. In some of the mathematical modeling, the magnetic forces have been used generally for improving the efficiency of the energy harvester. Some researchers have shown that the nonlinear oscillations of magnetic levitation can improve the energy harvesting ability under certain circumstances because of the wider range of vibration frequencies [13-14]. Various configurations and models have been used in mathematical modeling of magnetic forces by researchers. The magnetic forces can be introduced by analytical relations [15-17], identified polynomials [18] or by experiment [19].

One important aim in the development of nonlinear energy harvesters is to broaden the frequency bandwidth of energy harvesting. To this end, the advantages of the performance of nonlinear energy harvesting systems over traditional linear harvesters have been studied in the literature [20-21]. In order to improve the energy harvester performance, they have exploited the mechanical nonlinearities of the systems. Inserting the nonlinear terms of the physical model in mathematical modeling can reduce the error of numerical and experimental simulation results [15]. The primary sources of the nonlinearities are included geometric nonlinearities, damping, and elasticity [22, 23]. In the nonlinear systems, the chaos is a phenomenon that can occur in some conditions. The bandwidth of output power can be increased by inducing chaotic nonlinear phenomena and applying a low-



power controller [24]. Some researches [15, 25-28] has been developed to exploit the nonlinear behavior, especially chaotic motions in the energy harvesting systems. Another aspect of nonlinear energy harvesters is increasing the performance and enhancement of the frequency bandwidth, which is investigated by some researchers [29-32].

There are some works with a trapezoidal shape [33-36] that studied the shape parameters effects on frequencies and performance of the piezoelectric energy harvesters. Researches mentioned earlier show that there are varieties of respective works on rectangular beam (RB), but there is no work reported for the beam profile effects on the nonlinear dynamic behavior and performance of a vibratory piezo-magneto-elastic energy harvesting system. Therefore, studying the effect of the bimorph profile on the nonlinear dynamic behavior and performance of energy harvesting systems is one of the main contributions of this paper. Also, detecting the dominant behavior of the system in each case and their influence on output power are other contributions of this work.

The rest of this paper is arranged as follows: In Section 2, the dynamic modeling of a piezo-magneto-elastic energy harvesting system is derived. In Section 3, the nonlinear behavior analysis of the system is carried out to detect the chaotic behavior by utilizing suitable identifying techniques. Finally, summary and some concluding remarks are presented.

2. Dynamic Modeling of Piezomagnetoelastic Bimorph

Erturk and Inman [37] showed that, in a given frequency range, the piezomagnetoelastic energy harvesters could generate more energy than the common piezoelectric energy harvester. So the proposed model here is the piezomagnetoelastic energy harvester type. Figure 1 shows the energy harvesting system in this study. The proposed model consists of a trapezoidal bimorph (TB) and three permanent magnets with constant dimensions; and one of them, as a tip magnet, is mounted to the tip of the beam and the other two as external magnets, fixed to the base of the system with magnetically inert frame. The beam root and tip widths are characterized by b_0 and b_1 , respectively. The distance between the tip magnet and external magnets and the distance between the two external magnets are characterized by d_x and d_z , respectively.

The relative displacement vector of the beam element is given as

$$\mathbf{p}_r = [u - zw' \ 0 \ w]^T \quad (1)$$

where $u = u(x, t)$ and $w = w(x, t)$ are the longitudinal displacement and transverse displacement, respectively, and z is the vertical distance of the element from the neutral axis.

The velocity vector of the beam element is

$$\dot{\mathbf{p}} = [\dot{u} - z \dot{w}' \ 0 \ \dot{w} + \dot{z}_b]^T \quad (2)$$

where dot and prime symbols denote the differentiation with respect to time and space coordinate x , respectively, and z_b is the beam base excitation.

The total kinetic energy expression is as

$$T = \frac{1}{2} \int_{V_s} \rho_s \dot{\mathbf{p}}^T \dot{\mathbf{p}} dV_s + \frac{1}{2} \int_{V_{p1}} \rho_p \dot{\mathbf{p}}^T \dot{\mathbf{p}} dV_{p1} + \frac{1}{2} \int_{V_{p2}} \rho_p \dot{\mathbf{p}}^T \dot{\mathbf{p}} dV_{p2} + \frac{1}{2} M \dot{\mathbf{p}}_M^T \dot{\mathbf{p}}_M + \frac{1}{2} I_M \dot{w}'^2 \quad (3)$$

where the first term is the kinetic energy of the beam substructure, second and third are the lower and upper piezoelectric layers energy, and the two last terms are the tip mass translational and rotational elements energies, respectively. Also, ρ_s and ρ_p are the mass density of beam element and piezoelectric layer element, respectively; M , I_M and $\dot{\mathbf{p}}_M$ are mass, moment of inertia, and velocity vector of the tip magnet, respectively, where they are evaluated at location M .

The strain component is also expressed as follows:

$$\epsilon_{xx} = \frac{\partial p_r}{\partial x} i = \frac{\partial}{\partial x} (u - zw') = u' - zw'' \quad (4)$$

The isotropic substructure obeys Hooke's law

$$\sigma_{xx}^s = E_s \epsilon_{xx} = E_s (u' - zw'') \quad (5)$$

where E_s is the elastic modulus and σ_{xx}^s is the stress component.

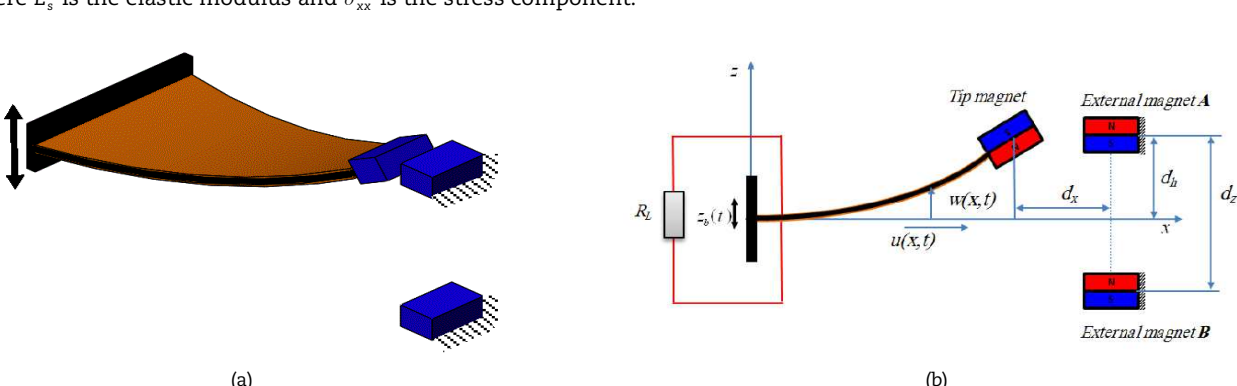


Fig. 1. Schematic of the vibratory energy harvesting system: (a) perspective view, (b) front view.

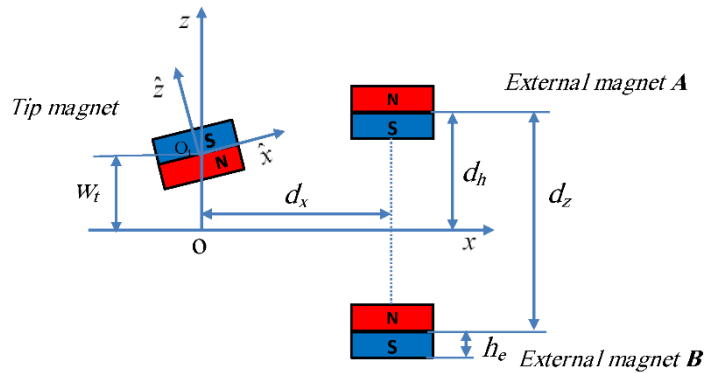


Fig. 2. Geometric configuration of the tip magnet and two external permanent magnets.

If one can model the behavior of the piezoelectric layer based on the Euler-Bernoulli beam theory as a thin beam, the stress components can be considered as a one-dimensional bending stress [37]. In this way, the stress-electrical displacement form of the reduced constitutive equations for a thin beam will be as follows:

$$\sigma_{xx}^p = E_p \varepsilon_{xx} - e_{31} E_3 \quad (6)$$

where e_{31} and E_p are the piezoelectric stress constant, reduced elastic modulus, respectively. The electric field is given in terms of the output voltage for the bimorph piezoelectric layer as $E_3 = -v(t) / 2h_p$, where $v(t)$ is the voltage across the electrodes and h_p is the thickness of the piezoelectric layer [37].

The total potential energy is given as

$$U = \frac{1}{2} \int_{V_s} E_s \varepsilon_{xx}^2 dV_s + \frac{1}{2} \int_{V_{p_1}} (E_p \varepsilon_{xx} - e_{31} E_3) \varepsilon_{xx} dV_{p_1} + \frac{1}{2} \int_{V_{p_2}} (E_p \varepsilon_{xx} - e_{31} E_3) \varepsilon_{xx} dV_{p_2} \quad (7)$$

Also, the internal electrical energy of the piezoelectric layers is obtained as [36]

$$\begin{aligned} W_e &= \frac{1}{2} \int_{V_{p_1}} \mathbf{E}^T \mathbf{D} dV_{p_1} + \frac{1}{2} \int_{V_{p_2}} \mathbf{E}^T \mathbf{D} dV_{p_2} \\ &= \frac{1}{2} \int_{V_{p_1}} E_3 (e_{31} \varepsilon_{xx} + \varepsilon_{33}^s E_3) dV_{p_1} + \frac{1}{2} \int_{V_{p_2}} E_3 (e_{31} \varepsilon_{xx} + \varepsilon_{33}^s E_3) dV_{p_2} \end{aligned} \quad (8)$$

where \mathbf{E} is the electric field vector components, $\mathbf{E} = [0 \ 0 \ E_3]^T$, and \mathbf{D} is the vector of electric displacement (dielectric) components, $\mathbf{D} = [0 \ 0 \ D_3]^T$ with $D_3 = e_{31} \varepsilon_{xx} + \varepsilon_{33}^s E_3$, where ε_{33}^s the is permittivity.

Figure 2 shows the geometric configuration of magnets. Magnetization of the tip magnet under an external magnetic field, as well as the magnetic force and moment applied on the tip magnet, can be obtained using the usual methods of permanent magnets. Here, a tip magnet and two permanent magnets are modeled with a charging model. In this model, the magnet is reduced to a distribution of equivalent magnetic charge, and also, a bipolar point approximation is used for Magnets [38].

The magnetic force created in the free space of two external magnets and at the point \mathbf{r} can be written as follows [39]

$$\mathbf{H}_{\text{ext}}(\mathbf{r}) = \frac{1}{4\pi} \sum_{i=1}^4 (-1)^i M_e \frac{\mathbf{r} - \mathbf{r}'_i}{|\mathbf{r} - \mathbf{r}'_i|^3} \quad (9)$$

where \mathbf{r}'_i is the position vector for the i^{th} equivalent point charge for external magnets and M_e is the magnetization of external magnets. The position vector relative to origin O can be written as follows

$$\begin{aligned} \mathbf{r}'_1 &= d_x \mathbf{i} + (d_h - h_e) \mathbf{k}, \quad \mathbf{r}'_2 = \mathbf{r}'_1 + 2h_e \mathbf{k} \\ \mathbf{r}'_3 &= d_x \mathbf{i} - (d_h + h_e) \mathbf{k}, \quad \mathbf{r}'_4 = \mathbf{r}'_3 + 2h_e \mathbf{k} \end{aligned} \quad (10)$$

where \mathbf{i} and \mathbf{k} represent the basis vectors in x and z directions, respectively. d_h and h_e are the distance of external magnet center from horizontal axes and half of external magnets height too.

In Eqs. (9) and (10), the quantities for $i = 1, 2$ are related to the negative and positive charge for the upper magnet, and the quantities $i = 3, 4$ are the same for the lower magnet.

The magnetization of the tip magnet has an angle to the horizontal axis. The magnetization \mathbf{M}_t is decomposed into two horizontal and vertical components. In this way, the tip magnet can be thought of as a pair of magnetic dipoles in directions \hat{x} and \hat{z} , respectively. Therefore, the magnetic forces and moments applied to each magnetic dipole can be calculated individually. Using the principle of superposition, we can obtain the resultant forces and moments imposed on the tip magnet [40, 15], which are defined as follows:

$$\mathbf{F} = \mu_0 \nabla (\mathbf{M}_t^T \mathbf{H}_{\text{ext}}(\mathbf{r}_k)) = \frac{\mu_0}{4\pi} \sum_{k=1}^4 \sum_{j=1}^4 (-1)^{k+j} M_t M_e \frac{\mathbf{r}_k - \mathbf{r}'_j}{|\mathbf{r}_k - \mathbf{r}'_j|^3} \quad (11)$$



$$\tau = \mu_0 \mathbf{M}_t \times \mathbf{H}_{ext}(\mathbf{r}_k) = \frac{\mu_0}{4\pi} \sum_{k=1}^2 \sum_{j=1}^4 (-1)^{k+j} M_t M_e \left(\mathbf{P}_k \times \frac{\mathbf{r}_k - \mathbf{r}'_j}{|\mathbf{r}_k - \mathbf{r}'_j|^3} \right) \quad (12)$$

where $\mu_0 = 4\pi \times 10^{-7} \text{Tm} / \text{A}$ is the permeability of free space; ∇ is the Del operator; \mathbf{M}_t is the magnetization of the tip magnet; \mathbf{r}_k is the position vector for the j^{th} equivalent point charge of the tip magnet; \mathbf{P}_k is the position vector from the origin of the body's coordinate system O_t to the j^{th} charging point where the moment is calculated around it. The position vectors \mathbf{r}'_j and \mathbf{P}_k can be written as

$$\begin{aligned} \mathbf{r}_1 &= \mathbf{r}_{O_t} - l_t \hat{\mathbf{i}}, \quad \mathbf{r}_2 = \mathbf{r}_{O_t} + l_t \hat{\mathbf{i}}, \quad \mathbf{r}_3 = \mathbf{r}_{O_t} - h_t \hat{\mathbf{k}}, \\ \mathbf{r}_4 &= \mathbf{r}_{O_t} + h_t \hat{\mathbf{k}}, \quad \mathbf{P}_k = \mathbf{r}_k - \mathbf{r}_{O_t} \quad (k = 1, 2, 3, 4) \\ \mathbf{r}_{O_t} &= u_t \hat{\mathbf{i}} + w_t \hat{\mathbf{k}}, \quad \hat{\mathbf{i}} = \mathbf{i} + w_{t,x} \mathbf{k}, \quad \hat{\mathbf{k}} = -w_{t,x} \mathbf{i} + \mathbf{k} \end{aligned} \quad (13)$$

where \mathbf{r}_{O_t} represent the position vector of the beam tip, and $\hat{\mathbf{k}}$ and $\hat{\mathbf{i}}$ represent the unit vectors in \hat{z} and \hat{x} directions, respectively. h_t and l_t are the height and length of the tip magnet, respectively, w_t and u_t are the lateral and longitudinal displacements of tip magnet, respectively, and $w_{t,x}$ is tip magnet angle. In Eqs. (11) - (13), the quantities for $k = 1, 2$ are related to negative and positive charges of the equivalent longitudinal dipole, respectively, and the quantities for $k = 3, 4$ are related to those of the vertical equivalent dipole for the tip magnet.

By replacing Eq. (13) in Eqs. (11) and (12), the force and momentum on the tip magnet are obtained as follows:

$$\mathbf{F} = f_{M_x} \mathbf{i} + f_{M_z} \mathbf{k} \quad (14)$$

$$\tau = \tau_{M_y} \mathbf{j} \quad (15)$$

$u(x,t)$ and $w(x,t)$ are the distributed-parameter variables in the mechanical domain and $v(t)$ is the electrical variable. On the other hand, the inextensibility of the beam yields the following relation between $u(x,t)$ and $w(x,t)$ [39,41]:

$$\frac{d}{dx}(u(x,t)) = \sqrt{1 - \left[\frac{d}{dx}(w(x,t)) \right]^2} - 1 \approx -\frac{1}{2} \left[\frac{d}{dx}(w(x,t)) \right]^2 \quad (16)$$

Therefore, $u(x,t)$ is expressed as follows

$$u(x,t) = -\frac{1}{2} \int_0^x \left[\frac{d}{ds}(w(s,t)) \right]^2 ds \quad (17)$$

The displacement field of the cantilever beam can expand as follows:

$$w(x,t) = \sum_{j=1}^n \psi_j(x) q_j(t) \quad (18)$$

where $\psi_j(x)$ are the admissible trial functions which satisfy the respective essential boundary conditions, $q_j(t)$ are the unknown generalized coordinates, and n is the number of modes considered for the solution. By substituting (18) into (17), the displacement field $u(x,t)$ is rewritten as

$$u(x,t) = -\frac{1}{2} \int_0^x \left[\sum_{j=1}^n \frac{d}{ds}(\psi_j(s)) q_j(t) \right]^2 ds = \sum_{i,j=1}^n R_{ij} q_i q_j \quad (19)$$

where $R_{ij} = -\frac{1}{2} \int_0^x \psi'_i(s) \psi'_j(s) ds$. Using Equations (18) and (19), the total kinetic and potential energy equations become

$$\begin{aligned} T &= 2 \int_{V_s} \rho_s \sum_{i,j,r,p=1}^n R_{ij} R_{rp} q_i q_r \dot{q}_j \dot{q}_p dV_s + \frac{1}{2} \int_{V_s} \rho_s z^2 \sum_{i,j=1}^n \psi'_i \psi'_j \dot{q}_i \dot{q}_j dV_s - 2 \int_{V_s} \rho_s z \sum_{i,j,r=1}^n R_{ij} \psi'_r q_i \dot{q}_j \dot{q}_r dV_s + \frac{1}{2} \int_{V_s} \rho_s \sum_{i,j=1}^n \psi_i \psi_j \dot{q}_i \dot{q}_j dV_s \\ &+ \int_{V_s} \rho_s \sum_{j=1}^n \psi_j \dot{q}_j \dot{z}_b dV_s + \frac{1}{2} \int_{V_s} \rho_s \dot{z}_b^2 dV_s + 2 \int_{V_{p_1}} \rho_{p_1} \sum_{i,j,r,p=1}^n R_{ij} R_{rp} q_i q_r \dot{q}_j \dot{q}_p dV_{p_1} + \frac{1}{2} \int_{V_{p_1}} \rho_{p_1} z^2 \sum_{i,j=1}^n \psi'_i \psi'_j \dot{q}_i \dot{q}_j dV_{p_1} - 2 \int_{V_{p_1}} \rho_{p_1} z \sum_{i,j,r=1}^n R_{ij} \psi'_r q_i \dot{q}_j \dot{q}_r dV_{p_1} \\ &+ \frac{1}{2} \int_{V_{p_1}} \rho_{p_1} \sum_{i,j=1}^n \psi_i \psi_j \dot{q}_i \dot{q}_j dV_{p_1} + \int_{V_{p_1}} \rho_{p_1} \sum_{j=1}^n \psi_j \dot{q}_j \dot{z}_b dV_{p_1} + \frac{1}{2} \int_{V_{p_1}} \rho_p \dot{z}_b^2 dV_{p_1} + 2 \int_{V_{p_2}} \rho_{p_2} \sum_{i,j,r,p=1}^n R_{ij} R_{rp} q_i q_r \dot{q}_j \dot{q}_p dV_{p_2} + \frac{1}{2} \int_{V_{p_2}} \rho_{p_2} z^2 \sum_{i,j=1}^n \psi'_i \psi'_j \dot{q}_i \dot{q}_j dV_{p_2} \\ &- 2 \int_{V_{p_2}} \rho_{p_2} z \sum_{i,j,r=1}^n R_{ij} \psi'_r q_i \dot{q}_j \dot{q}_r dV_{p_2} + \frac{1}{2} \int_{V_{p_2}} \rho_{p_2} \sum_{i,j=1}^n \psi_i \psi_j \dot{q}_i \dot{q}_j dV_{p_2} + \int_{V_{p_2}} \rho_{p_2} \sum_{j=1}^n \psi_j \dot{q}_j \dot{z}_b dV_{p_2} + \frac{1}{2} \int_{V_{p_2}} \rho_p \dot{z}_b^2 dV_{p_2} \\ &+ \frac{1}{2} M \left[4 \sum_{i,j,r,p=1}^n R_{ij} R_{rp} (L) q_i q_r \dot{q}_j \dot{q}_p + \sum_{i,j=1}^n \psi_i(L) \psi_j(L) \dot{q}_i \dot{q}_j + 2 \sum_{i=1}^n \psi_i(L) \dot{q}_i \dot{z}_b + z_b^2 \right] + \frac{1}{2} I_M \sum_{i,j=1}^n \psi'_i(L) \psi'_j(L) \dot{q}_i \dot{q}_j \end{aligned} \quad (20)$$



$$\begin{aligned}
U = & \frac{1}{2} \int_{V_s} E_s \left(\frac{1}{4} \sum_{i,j,r,p=1}^n \psi_i' \psi_j' \psi_r' \psi_p' q_i q_j q_r q_p + z^2 \sum_{i,j=1}^n \psi_i'' \psi_j'' q_i q_j + z \sum_{i,j,r=1}^n \psi_i' \psi_j' \psi_r' q_i q_j q_r \right) dV_s \\
& + \frac{1}{2} \int_{V_{p_1}} E_{p_1} \int_{V_s} E_s \left(\frac{1}{4} \sum_{i,j,r,p=1}^n \psi_i' \psi_j' \psi_r' \psi_p' q_i q_j q_r q_p + z^2 \sum_{i,j=1}^n \psi_i'' \psi_j'' q_i q_j + z \sum_{i,j,r=1}^n \psi_i' \psi_j' \psi_r' q_i q_j q_r \right) dV_{p_1} \\
& + \frac{1}{4} \int_{V_{p_1}} e_{31} E_3 \left(\sum_{i,j=1}^n \psi_i' \psi_j' q_i q_j \right) dV_{p_1} + \frac{1}{2} \int_{V_{p_1}} e_{31} E_3 z \sum_{i=1}^n \psi_i'' q_i dV_{p_1} \\
& + \frac{1}{2} \int_{V_{p_2}} E_{p_2} \left(\frac{1}{4} \sum_{i,j,r,p=1}^n \psi_i' \psi_j' \psi_r' \psi_p' q_i q_j q_r q_p + z^2 \sum_{i,j=1}^n \psi_i'' \psi_j'' q_i q_j + z \sum_{i,j,r=1}^n \psi_i' \psi_j' \psi_r' q_i q_j q_r \right) dV_{p_2} \\
& + \frac{1}{4} \int_{V_{p_2}} e_{31} E_3 \left(\sum_{i,j=1}^n \psi_i' \psi_j' q_i q_j \right) dV_{p_2} + \frac{1}{2} \int_{V_{p_2}} e_{31} E_3 z \sum_{i=1}^n \psi_i'' q_i dV_{p_2}
\end{aligned} \tag{21}$$

$$\begin{aligned}
W_e = & -\frac{1}{4} \int_{V_{p_1}} e_{31} E_3 \left(\sum_{i,j=1}^n \psi_i' \psi_j' q_i q_j \right) dV_{p_1} - \frac{1}{2} \int_{V_{p_1}} e_{31} E_3 z \sum_{i=1}^n \psi_i'' q_i dV_{p_1} + \frac{1}{2} E_3^2 \varepsilon_{33}^s V_{p_1} \\
& -\frac{1}{4} \int_{V_{p_2}} e_{31} E_3 \left(\sum_{i,j=1}^n \psi_i' \psi_j' q_i q_j \right) dV_{p_2} - \frac{1}{2} \int_{V_{p_2}} e_{31} E_3 z \sum_{i=1}^n \psi_i'' q_i dV_{p_2} + \frac{1}{2} E_3^2 \varepsilon_{33}^s V_{p_2}
\end{aligned} \tag{22}$$

By using the matrices defined in appendix A, equations (20) to (22) can be rewritten as

$$T = \frac{1}{2} \sum_{i,j=1}^n M_{ij} \dot{q}_i \dot{q}_j + \sum_{i=1}^n H_i \dot{q}_i \dot{z}_b + \frac{1}{2} M_T \dot{z}_b^2 \tag{23}$$

$$U = \frac{1}{2} \sum_{i,j=1}^n K_{ij} q_i q_j + \frac{1}{2} \sum_{i=1}^n E_3 G_i q_i \tag{24}$$

$$W_e = -\frac{1}{2} \sum_{i=1}^n E_3 G_i q_i + \frac{1}{2} E_3^2 \varepsilon_{33}^s (V_{p_1} + V_{p_2}) \tag{25}$$

It should be noted $M_{ij} = M_{ij}(\mathbf{q})$, $K_{ij} = K_{ij}(\mathbf{q})$, and $G_i = G_i(\mathbf{q})$. Electromechanical Lagrange equations are expressed as follows:

$$\begin{aligned}
\frac{d}{dt} \left(\frac{\partial T}{\partial \dot{q}_k} \right) - \frac{\partial T}{\partial q_k} + \frac{\partial U}{\partial q_k} - \frac{\partial W_e}{\partial q_k} &= Q_k \quad \& k = 1, 2, \dots, n \\
\frac{d}{dt} \left(\frac{\partial T}{\partial v} \right) - \frac{\partial T}{\partial v} + \frac{\partial U}{\partial v} - \frac{\partial W_e}{\partial v} &= Q_e
\end{aligned} \tag{26}$$

where Q_k and Q_e are the generalized forces and the electric charge output of the piezoelectric layer, respectively. One can obtain these forces by the virtual work of the mechanical force and electric charge as follows:

$$\delta W_{nc} = Q_e \delta v + F_{M_x} \delta u_t + F_{M_z} \delta w_t + \tau_{M_y} \delta w_t' \tag{27}$$

where $\dot{Q}_e = v / R_l$ is the electric charge output of the piezoelectric layers, and $u_t = u(L, t)$, $w_t = w(L, t)$, $w_t' = \frac{\partial w(x, t)}{\partial x} \Big|_{x=L}$ are the longitudinal, transverse, and rotational displacements of the beam tip, respectively. Now, equation (26) yields the equations of motion as

$$\begin{aligned}
& \sum_{j=1}^n M_{kj} \ddot{q}_j + \sum_{j=1}^n \dot{M}_{kj} \dot{q}_j - \frac{1}{2} \sum_{i,j=1}^n M_{ij,k} \dot{q}_i \dot{q}_j + \frac{1}{2} \left(\sum_{i,j=1}^n K_{ij,k} q_i q_j + \sum_{j=1}^n K_{jk} q_k + \sum_{j=1}^n K_{kj} q_k \right) \\
& + \sum_{j=1}^n E_3 G_{j,k} q_j + E_3 G_k + H_k \ddot{z}_b = f_{m_z} \psi_k(l) + \tau_m \psi_k'(l) \quad \& k = 1, 2, \dots, n \\
& \frac{\varepsilon_{33}^s}{4h^2} (V_{p_1} + V_{p_2}) \dot{v} + \frac{\nu}{R_l} - \frac{1}{2h} \sum_{i,j=1}^n G_{i,j} q_i \dot{q}_j - \frac{1}{2h} \sum_{i=1}^n G_i q_i = 0
\end{aligned} \tag{28}$$

where the matrices $\mathbf{M} = \mathbf{M}(\mathbf{q}) \in \mathbb{R}^{n \times n}$, $\mathbf{K} = \mathbf{K}(\mathbf{q}) \in \mathbb{R}^{n \times n}$, $\mathbf{G} = \mathbf{G}(\mathbf{q}) \in \mathbb{R}^n$ and $\mathbf{H} \in \mathbb{R}^n$ are defined in Appendix A. Thereby, the vibrational and electrical equations are derived. It is seen that the equations of motion (28) are nonlinear in terms of the generalized coordinates.

3. Simulation Results and Discussion

Before conducting the numerical analysis for the proposed continuous model, the validity of the model is verified by previously published experimental results. The validity of bimorph, that composed of the main base structure and two upper and lower piezoelectric layers, is performed by the experimental result presented in [42]. The harvested steady-state voltage versus amplitude of the exciting acceleration for the current model and the experimental model are being compared. As shown in Fig. 3(a), there is good accordance, especially in the low exciting acceleration (about 0.2g for the current model). The validity of



magnetic forces comprising tip magnet and two external magnets of the current model is verified by the experimental results presented in [18]. The magnetic forces versus vertical displacement of tip magnet are plotted in Fig. 3(b), which reveals the good accordance between the current model and the experimental model. So, it can rely on the proposed dynamic model and equations of motion. The numerical analysis to investigate the dynamic behavior can be followed by details.

Numerical solution of nonlinear differential equations, Eq. (28), is done by Runge–Kutta numerical method with variable steps in MATLAB software. To ensure that the data used in numerical analysis is in a steady state conditions, a large amount first time series data of integration has been excluded. The results of the next time series data of integration are kept to carry out the analysis. The numerical values of the energy harvesting system parameters used in the numerical analysis are given in Table 1. Also, the frequency and amplitude of the exciting acceleration in all numerical simulations are chosen as 10Hz and 2mm/s², respectively. The nonlinear analysis is conducted in two following cases: trapezoidal bimorph with small tip width and trapezoidal bimorph with small root width, namely TBST and TBSR, respectively.

3.1 Nonlinear analysis of TBST

To investigate the nonlinear dynamic behavior of the system by numerical methods, some identifying techniques are required. The bifurcation diagrams are one of the main tools to analyze the nonlinear dynamic behavior of the systems. These diagrams can be useful in detecting the irregular regions (quasi-periodic or chaotic) of the system behavior under the influences of some parameters. The gap distance between two external magnets, d_z , and the separation distance between the tip magnet and the external magnets, d_x , are used as a control parameters in the bifurcation diagrams. In this case, the beam root width is higher than the beam tip width.

Figure 4 shows the bifurcation diagram for TBST ($b_0 = 0.02m$, $b_1 = 0.01m$). At parameter range $d_x = [0.075m \sim 0.089m]$, the dynamic behavior is periodic with some jumping phenomenon, which is one of the phenomena occurring in nonlinear systems. In this range, the harvested voltage is about zero. At range, $d_x = [0.0895m \sim 0.09m]$ the system behavior is subharmonic (3T), where the maximum lateral displacement and output power are 0.067m and 4.898 milliwatt (mW), respectively. After here, up to 0.0945m, the motion again returns to periodic, and the output voltage is not considerable. In the region $d_x = [0.095m \sim 0.104m]$ there is an irregular motion; beam tip displacements are relatively high, and output power is higher than the periodic region, but it is lower than the subharmonic motions. It should be noted that in this region there are some periodic motions with relatively small displacements, where the output power is higher than the previous periodic regions. By increasing the bifurcation parameter, excepting of two irregular regions at $d_x = 0.1075m$ and $d_x = 0.1085m$, the motion returns to periodic and remains in this state up to the end of the region.

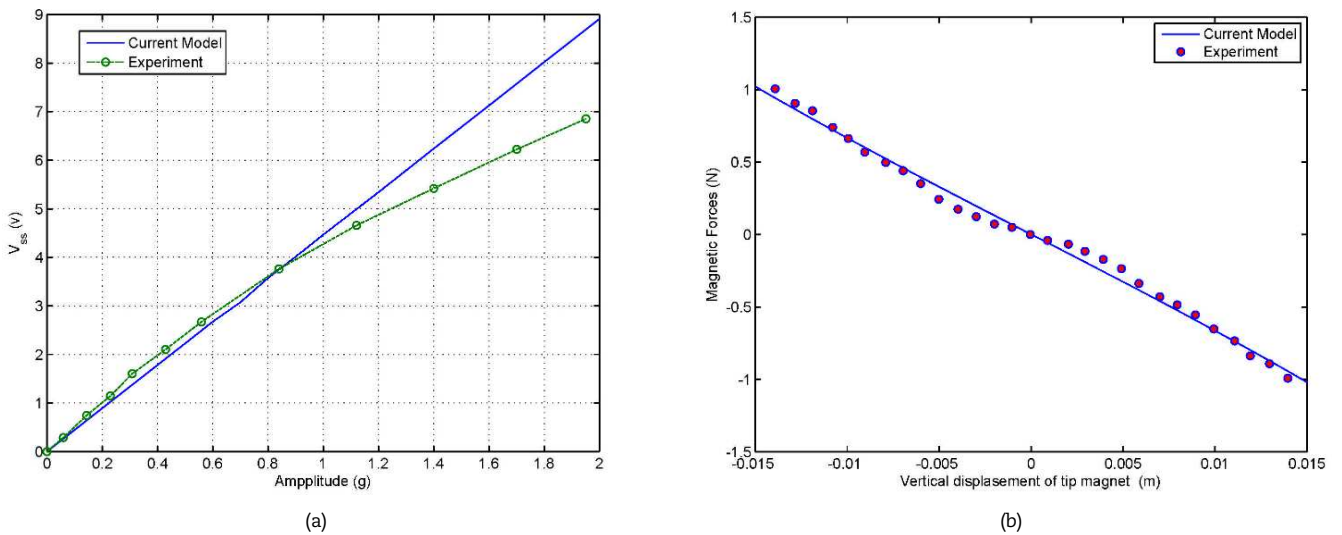


Fig. 3. Dynamic model verification of (a) bimorph, (b) magnetic forces.

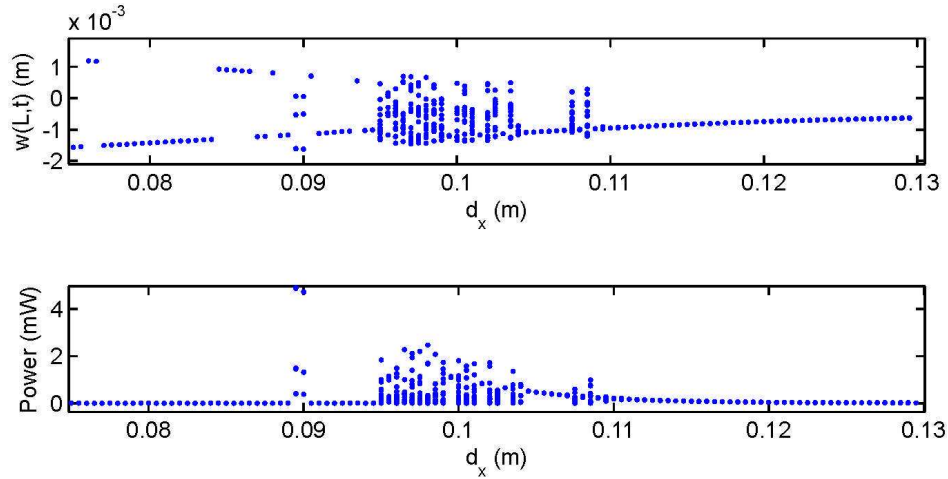
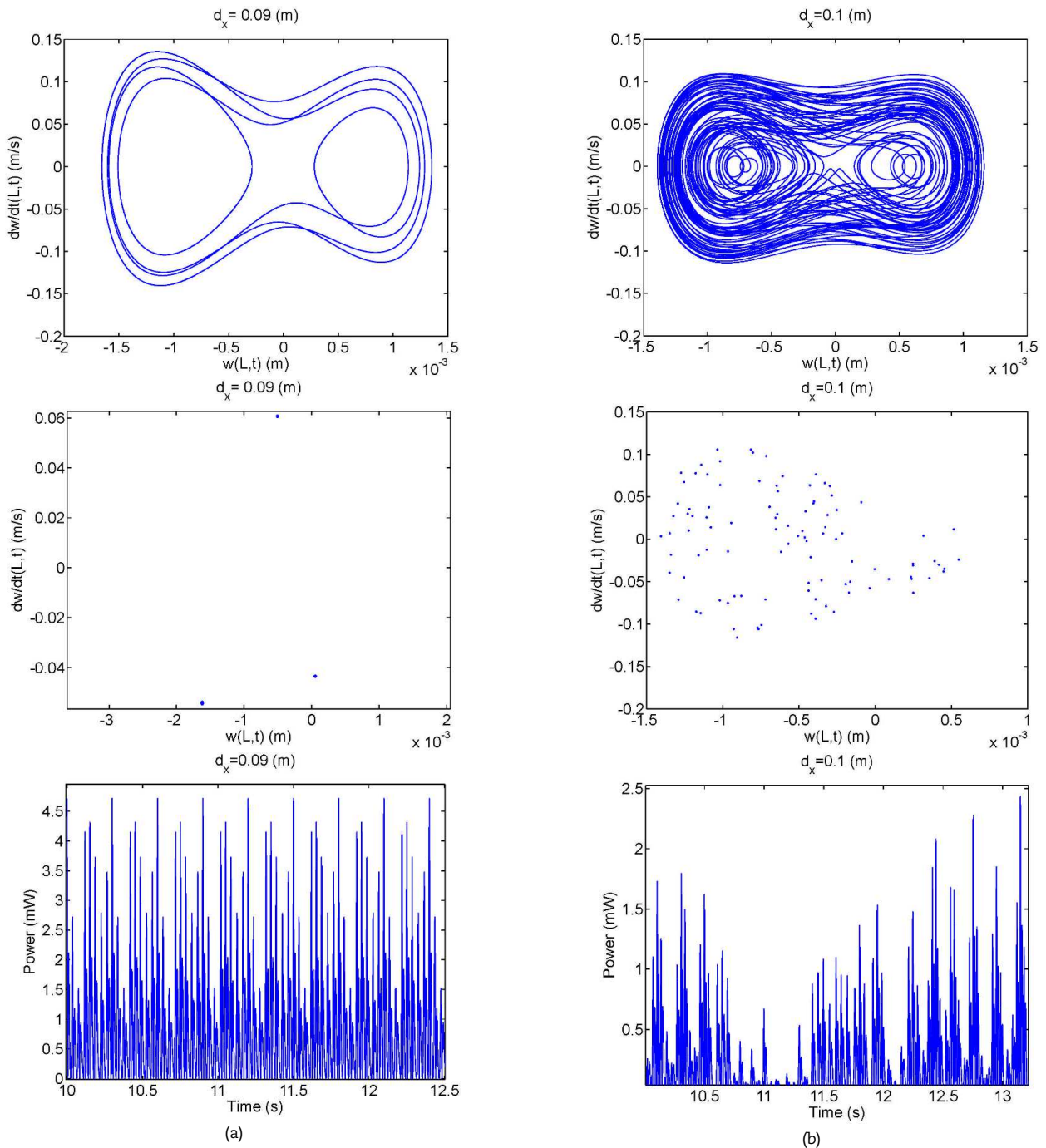


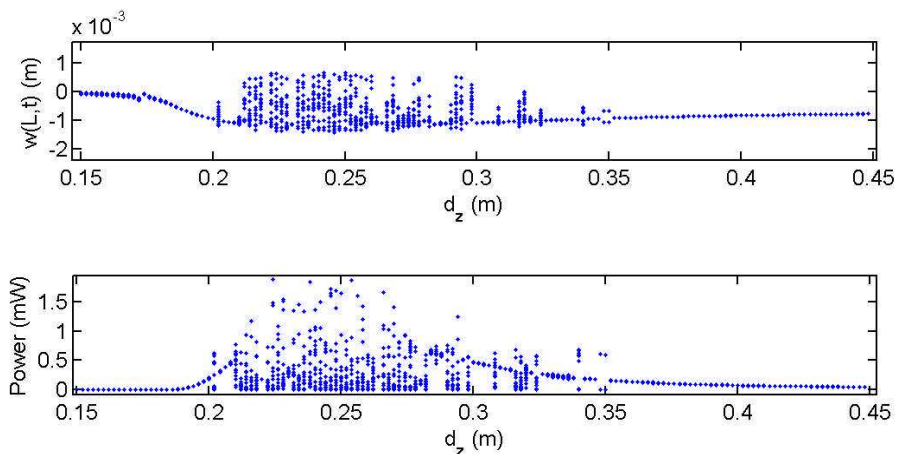
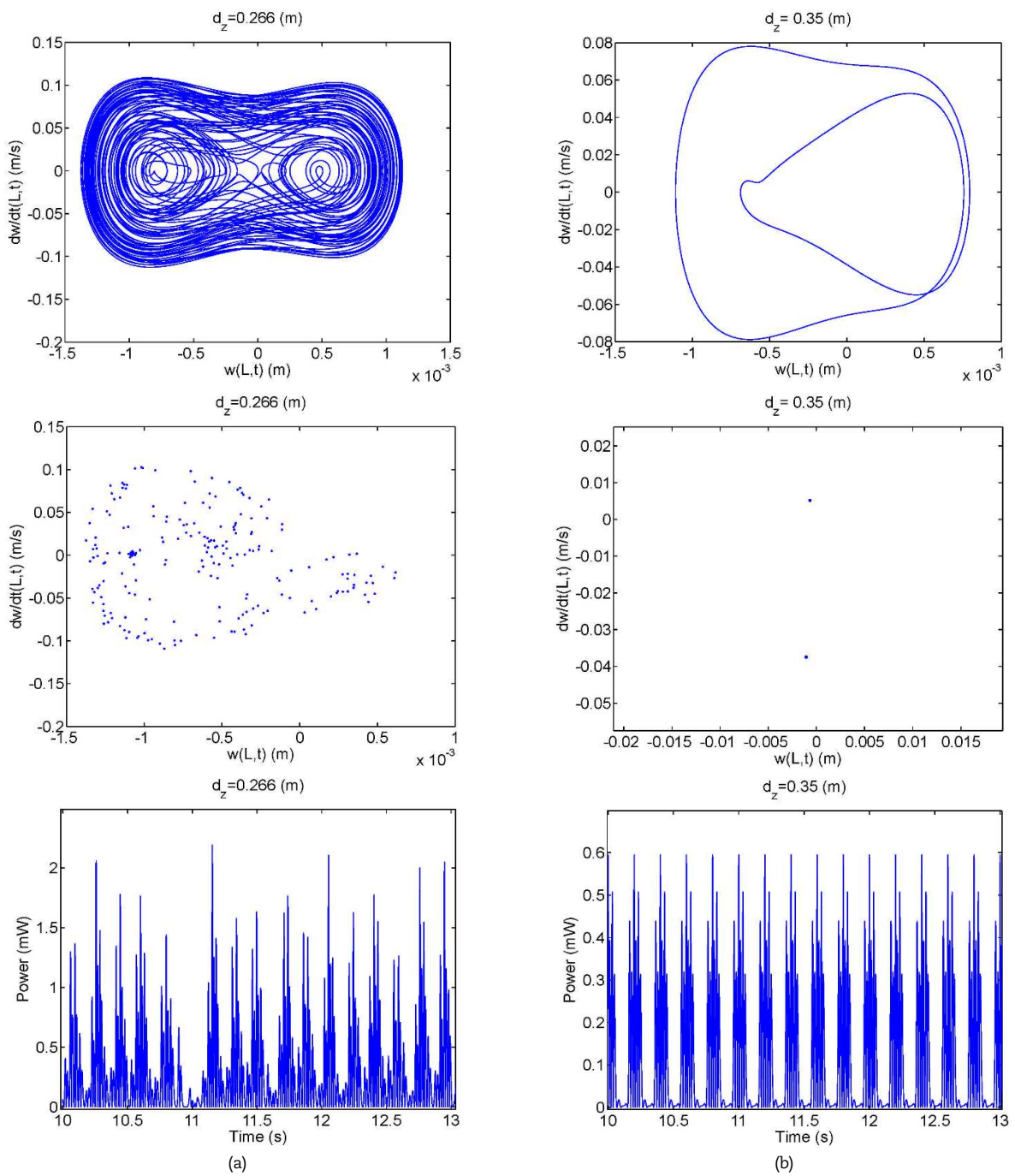
Fig. 4. Bifurcation diagrams for TBST with the control parameter d_x .



Table1. Parameters value of piezomagnetoelastic bimorph

Parameter value	Description
$L = 100 \text{ mm}$	Length of the beam
$b = 6.4 \text{ mm}$	Width of the beam
$h_s = 0.14 \text{ mm}$	Thickness of the beam
$\rho_s = 9000 \text{ kg / m}^3$	Mass density of the beam
$E_s = 105 \text{ Gpa}$	Young's modulus of the beam
$h_p = 0.265 \text{ mm}$	The thickness of the piezoelectric layers
$\rho_p = 7500 \text{ kg / m}^3$	The mass density of the piezoelectric layers
$e_{31} = -16.6 \text{ C / m}^2$	Piezoelectric constant
$\epsilon_{33}^s = 25.55 \text{ nF / m}$	Permittivity
$E_p = 60.6 \text{ Gpa}$	Young's modulus of the piezoelectric layers
$\rho_M = 7400 \text{ kg / m}^3$	Mass density of the tip magnet
$\mu_0 = 4\pi \times 10^{-7} \text{ N / A}^2$	Magnetic constant
$R_l = 100 \text{ k}\Omega$	Resistance load

**Fig. 5.** Validation of bifurcation diagram by phase plane, Poincare map, and output power time series for (a) periodic, (b) chaotic.

**Fig. 6** Bifurcation diagrams for TBST with the control parameter d_z .**Fig. 7.** Validation of bifurcation diagram by phase plane, Poincaré map and output power time series for (a) chaotic, (b) periodic

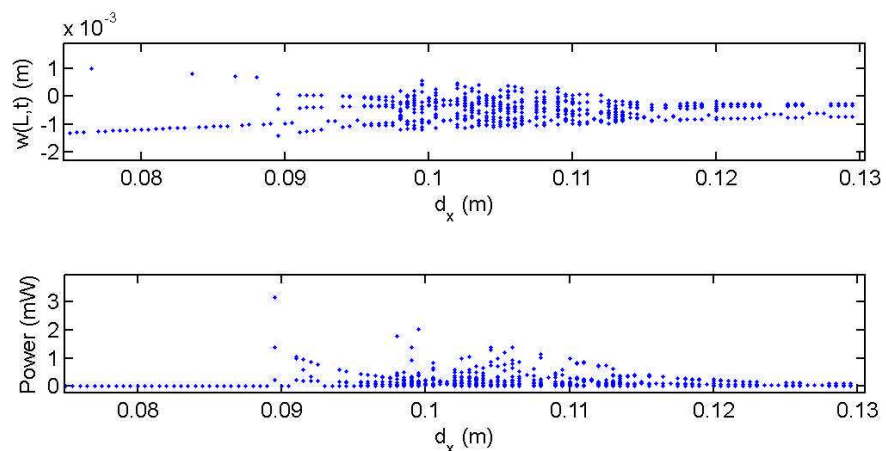


Fig. 8. Bifurcation diagrams for TBSR with the control parameter d_x .

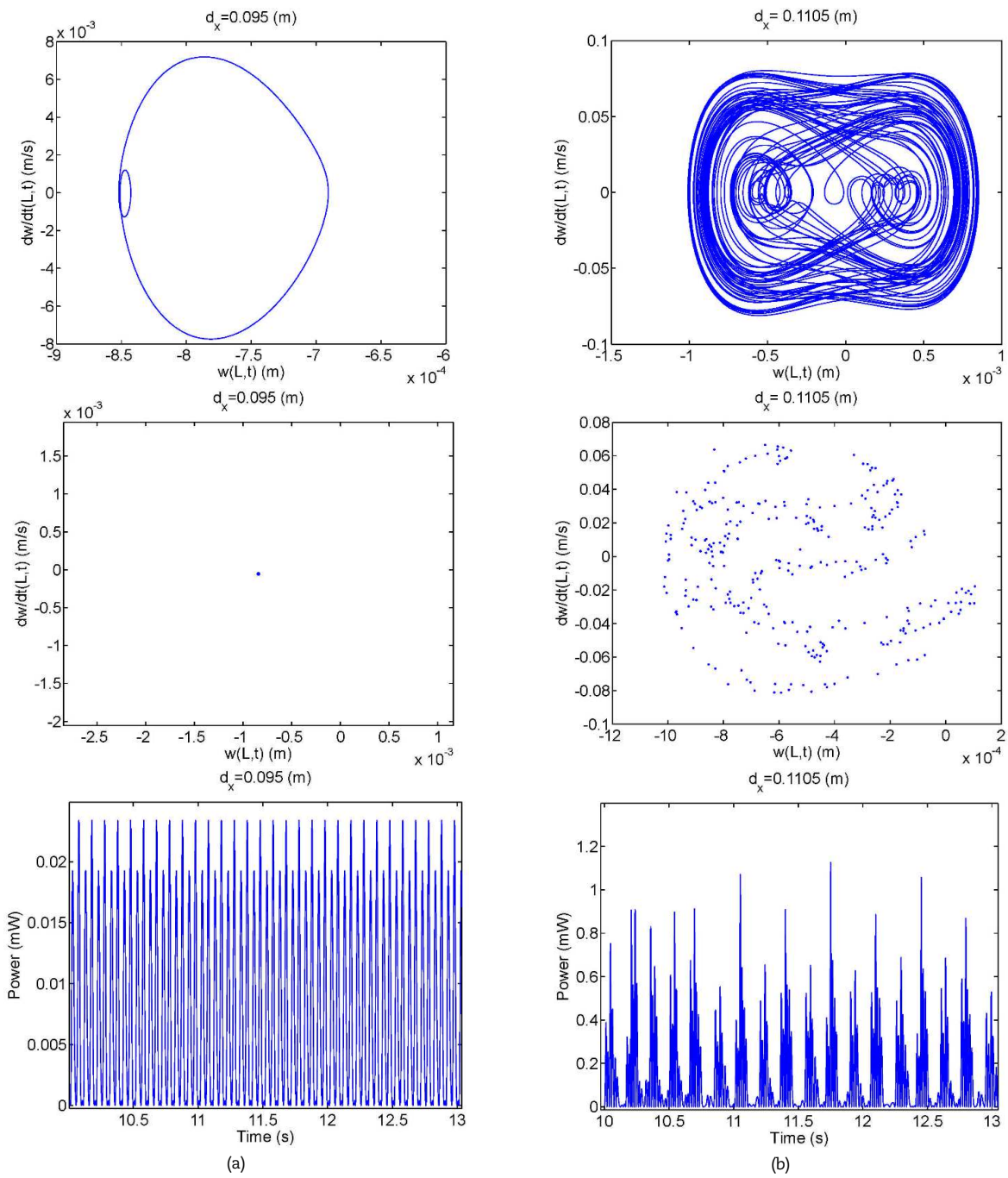


Fig. 9. Validation of bifurcation diagram by phase plane, Poincaré map, and output power time series for (a) periodic, (b) chaotic.



To confirm the captured behavior on the bifurcation diagrams, two typical points are selected for detailed analysis by other identifying techniques. Here, the phase plane portrait and Poincare map are used to attain the object. As shown in Fig. 5, the motion is subharmonic (3T) and chaotic at $d_x = 0.09m$ and $d_x = 0.1m$, respectively. Also, Fig. 5(c) shows the output power at the two mentioned points. It can be seen that the power in subharmonic motion is higher than the chaotic motion for this case.

As shown in Fig. 6, the bifurcation diagram is established by changing the separation distance between two external magnets. By increasing the separation distance up to $d_z = 0.2m$, both the beam tip displacements and harvested voltage are gradually increased. At region $d_z = [0.2m\sim0.298m]$, the dominant behavior is chaotic. The motion between $d_z = 0.3m$ to $d_z = 0.346m$ is periodic (T) or irregular. At region $d_z = [0.348m\sim0.35m]$, the motion is subharmonic with relatively higher output power. After this, the motion is periodic, and both tip displacements and power decrease.

As shown in Fig. 7(a), the phase plane portrait has many crossings, and the Poincare map has a fractal structure at $d_z = 0.266m$, that confirms the chaotic motion. Also, two crossings on the phase plane and two separate points on the Poincare map in Fig. 7(b) represent the subharmonic (2T) motion at $d_z = 0.35m$. As illustrated in Fig. 7, in this case, the extracted power for chaotic motion is higher than the subharmonic one.

3.2 Nonlinear analysis of TBSR

In this section, the BCTBSR ($b_0 = 0.01m$ and $b_1 = 0.02m$) profile is studied. As in the previous section, the bifurcation diagrams are used to analyze the dynamic behavior. Also, the separation distance d_z and gap distance d_x are used as a bifurcation control parameters. Figure 8 shows the bifurcation diagram for this case, where the distance of the gap is used as the control parameter. In comparison with Fig. 4, the dynamic behavior of the system in the first region, $d_x = [0.075m\sim0.089m]$, has not shown considerable changes, but after this region and up to $d_x = 0.0975m$ the most dominant behavior is subharmonic. At $d_x = 0.098m$ the motion falls into irregular behavior up to $d_x = 0.1145m$. The dominant behavior in the last region is subharmonic, with relatively lower harvested voltage.

As shown in Figs. 9(a) and 9(b), the motion is periodic at $d_x = 0.095m$ and chaotic at $d_x = 0.1105m$, respectively. The power extracted at these two points is also shown in the Figs. 9(a) and 9(b), where the power values for chaotic motion is higher than the periodic one.

As shown in Fig. 10, when the separation distance between two external magnets is chosen as a bifurcation parameter, up to $d_z = 0.186m$, the beam tip has negligible deflections, and output power is about zero. By increasing d_z the motion bifurcates to subharmonic behavior (3T), where both the displacement and output power are increasing. The two relatively broadband irregular regions at ranges $d_z = [0.196m\sim0.262m]$ and $d_z = [0.282m\sim0.396m]$ can be seen, where the highest harvested power was attained in the first region. In the second irregular region, the beam tip deflections and output power begin to decrease. The most dominant behavior between two irregular regions and the last region is subharmonic with medium power.

Two typical points are selected to confirm the captured data on bifurcation diagrams. The phase portrait has many crossings, and the Poincare map has discernible fractal structure in Fig. 11(a) that is indicative of a strange attractor at $d_z = 0.242m$. Hence this attractor is chaotic. The finite crossing and discrete points (5 points) at $d_z = 0.382m$ in Fig. 11(b) are indicative of subharmonic (5T) motions. Also, it is seen that the maximum output power in the chaotic motion is higher than the subharmonic one on respective points.

3.3 Output power comparison of rectangular and trapezoidal bimorph

One of the main goals in the energy harvesting system is to reach the higher performance by increasing the output power. There are various methods to improve the harvester performance that are studied by many researchers, and some of them are mentioned in Section 1. Here, the effect of the beam profile is studied. Although the beam profile can influence the dynamic behavior of the system, the output power has great importance in energy harvesting systems. So this section is assigned only to harvested power values due to the change in the beam profile. To this end, a typical point, $d_x = 0.1m$ and $d_z = 0.232m$, in a chaotic region, is selected to perform analysis. Fig. 12 shows the maximum harvested voltage for three cases. In the first case, Fig. 12(a), the beam profile is RB, $b_0 = b_1 = 0.02m$. In this case, for a typical point, the output power is 1.336 (mW). In the second case, ($b_0 = 0.02m$, $b_1 = 0.01m$), the beam profile is TBST. In this case, in Fig. 12(b), the maximum harvested power is 2.436 (mW). In the third case ($b_0 = 0.01m$, $b_1 = 0.02m$), the beam is TBSR. In this case, in Fig. 12(c), the maximum output power is 1.853 (mW). The performed analysis for some other typical points shows the same results. The comparison between the three cases shows that the beam with a rectangular profile has the lowest, and the trapezoidal profile with small tip width has the highest output power.

3.4 Effect of tip and root widths on nonlinear behavior

The analysis of the previous section shows that by using the trapezoidal beam profile, the harvested power values can be improved. In this section, the effect of two important geometric parameters (i.e., beam tip and root widths, b_1 and b_0 , respectively) is investigated. Here, the separation distance between two external magnets and the gap distance between tip magnet and external magnets are chosen as $d_x = 0.092m$, $d_z = 0.192m$, where the motion is periodic. In the first case, the beam root width is used as a bifurcation parameter, and the beam tip width is constant. As shown in Fig. 13, by changing b_0 , the periodic attractor can be converted to subharmonic or strange attractors.

As mentioned previously, the bifurcation diagrams can only give the overall view of the system's dynamic behavior, particularly in irregular regions. In these regions, it is not possible to distinguish between quasi-periodic or chaotic motions. So there is a need for other investigation techniques to confirm the bifurcation results. Two typical points on the bifurcation diagram are chosen for detailed analysis. At $b_0 = 0.012m$, Fig. 14 (a), the phase portrait has finite crossings, and the Poincare map shows six single points that confirm the subharmonic (6T) motion. At $b_0 = 0.01m$, the phase plane shows many crossings, and in Poincare map, the points spread throughout the plane (see Fig. 14(b)), and this confirms the chaotic motion at $b_0 = 0.01m$. Also, figure 14 shows that the maximum output power in these two points is 0.14 (mW) and 0.45 (mW) for subharmonic and chaotic motions, respectively.

In the second case, the beam tip width b_1 is used as the bifurcation parameter, and the beam root width b_0 is constant. In this case, by changing b_1 , as shown in Fig. 15, the behavior is subharmonic or irregular. As it is seen, the periodic motion is relatively high, and irregular regions spread throughout the domain.

In order to confirm the bifurcation diagram, other techniques are used in two points $b_1 = 0.0064m$ and $b_1 = 0.0146m$. As shown in Fig. 16(a), Poincare map, and phase portrait confirm the periodic (1T) motion in $b_1 = 0.0064m$. Also, many crossing in phase portrait and fractal structure in Fig. 16 (b) indicate the chaotic motion for $b_1 = 0.0146m$. The maximum output power for $b_1 = 0.0064m$ and $b_1 = 0.0146m$ are 0.15 (mW) and 2.167 (mW), respectively.

All of the previous analysis conducted was based on the constant exciting frequency and changing some parameters. Here, the waterfall diagrams are used to give better insight on simultaneous changes of the exciting frequency and respective bifurcation parameters. As shown in Fig. 17, one can obtain a higher voltage in the exciting frequency 34 (Hz). Also, these waterfalls show that the output voltage increases by decreasing the respective parameters.



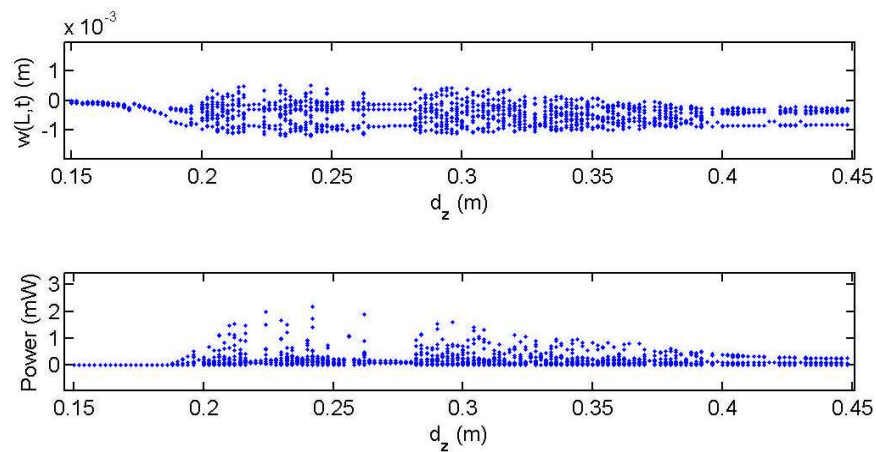


Fig. 10. Bifurcation diagrams for TBSR with control parameter d_z .

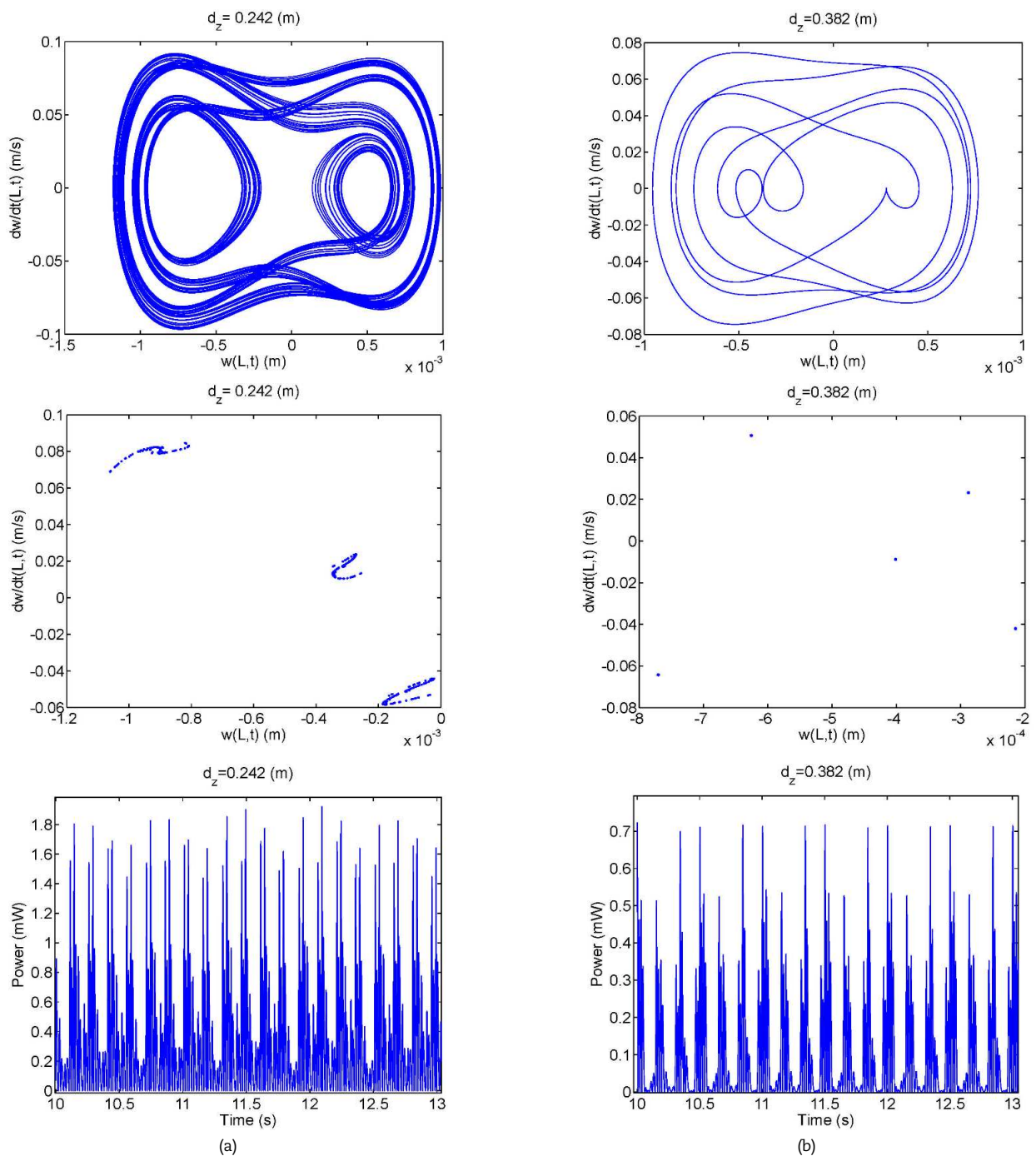


Fig. 11. Validation of bifurcation diagram by phase plane, Poincare map and output power time series for (a) at chaotic, (b) subharmonic



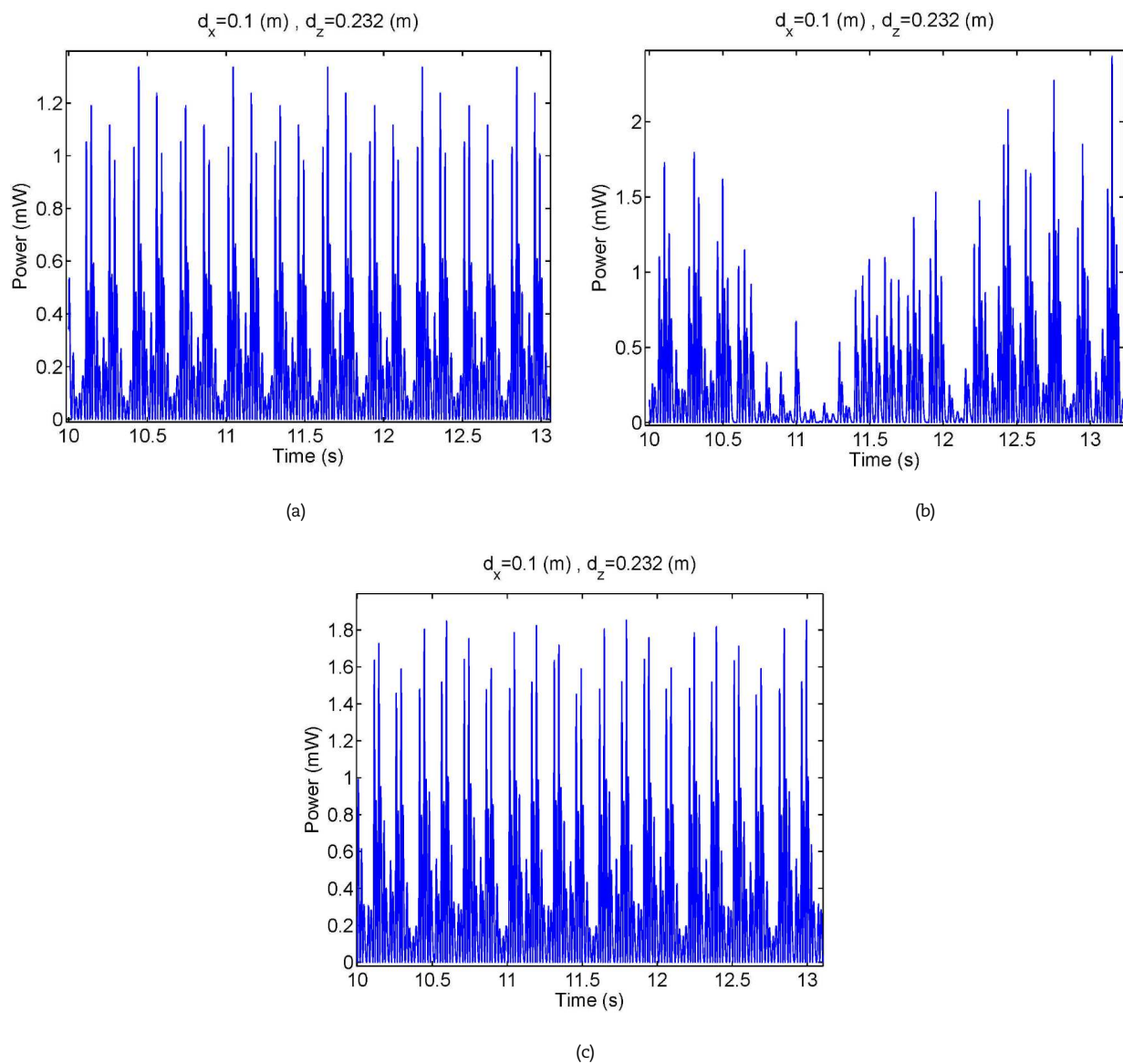


Fig. 12. Maximum harvested power at $d_x = 0.1\text{m}$ and $d_x = 0.232\text{m}$ for: (a) RB profile, (b) TBST profile, (c) TBSR profile.

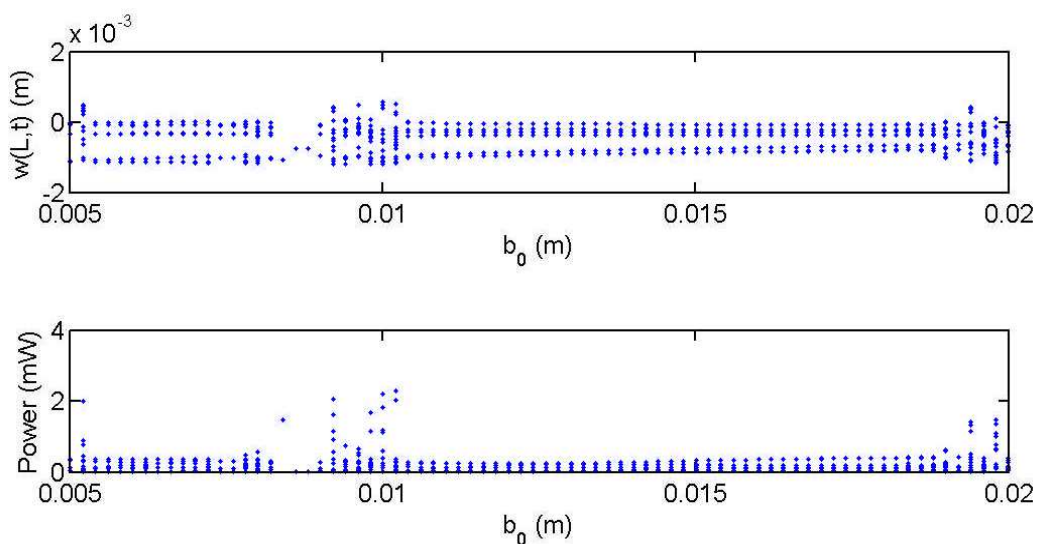


Fig. 13. Bifurcation diagrams for TB with $b_1 = 0.02\text{m}$, $d_x = 0.092\text{m}$ and $d_z = 0.192\text{m}$ and control parameter b_0 .



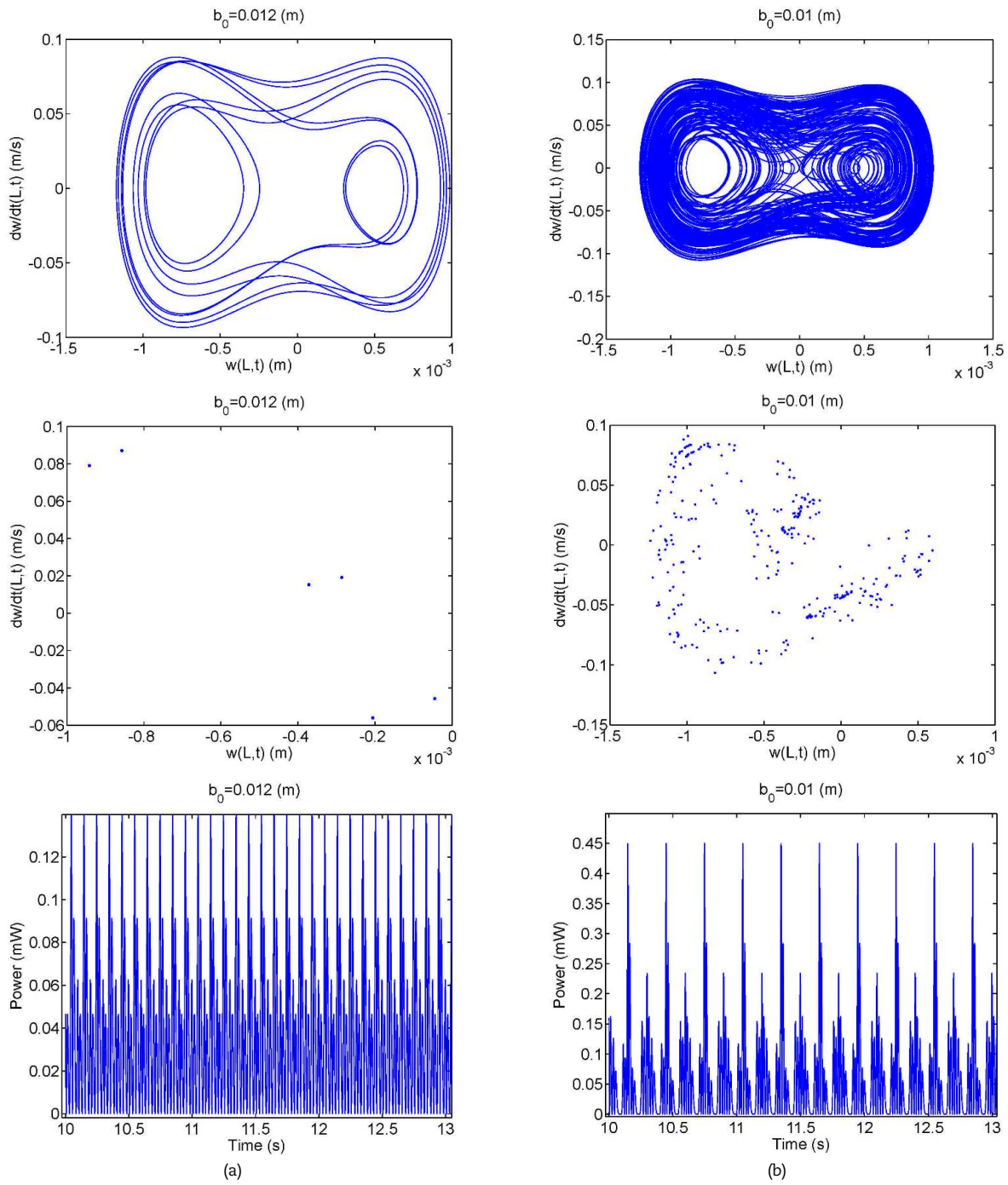


Fig. 14. Validation of bifurcation diagram by phase plane, Poincare map, and output power time series for (a) at chaotic, (b) subharmonic.

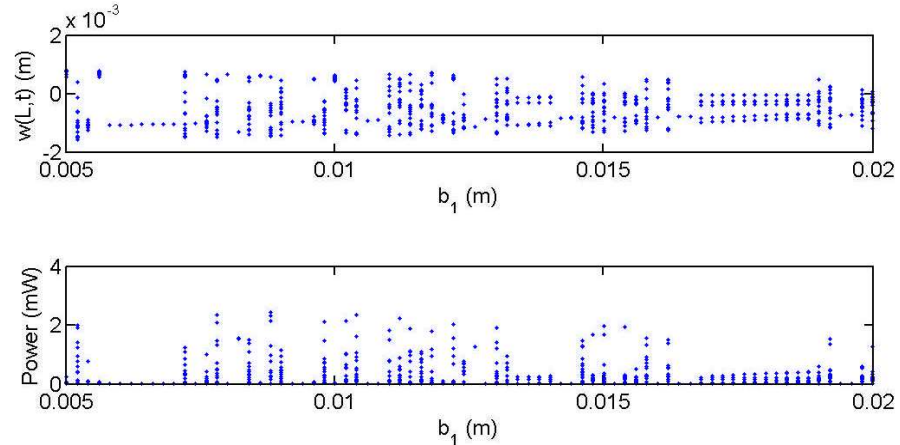


Fig. 15 Bifurcation diagrams for TB with $b_0 = 0.02$ m, $d_x = 0.092$ m and $d_z = 0.192$ m and control parameter b_1 .



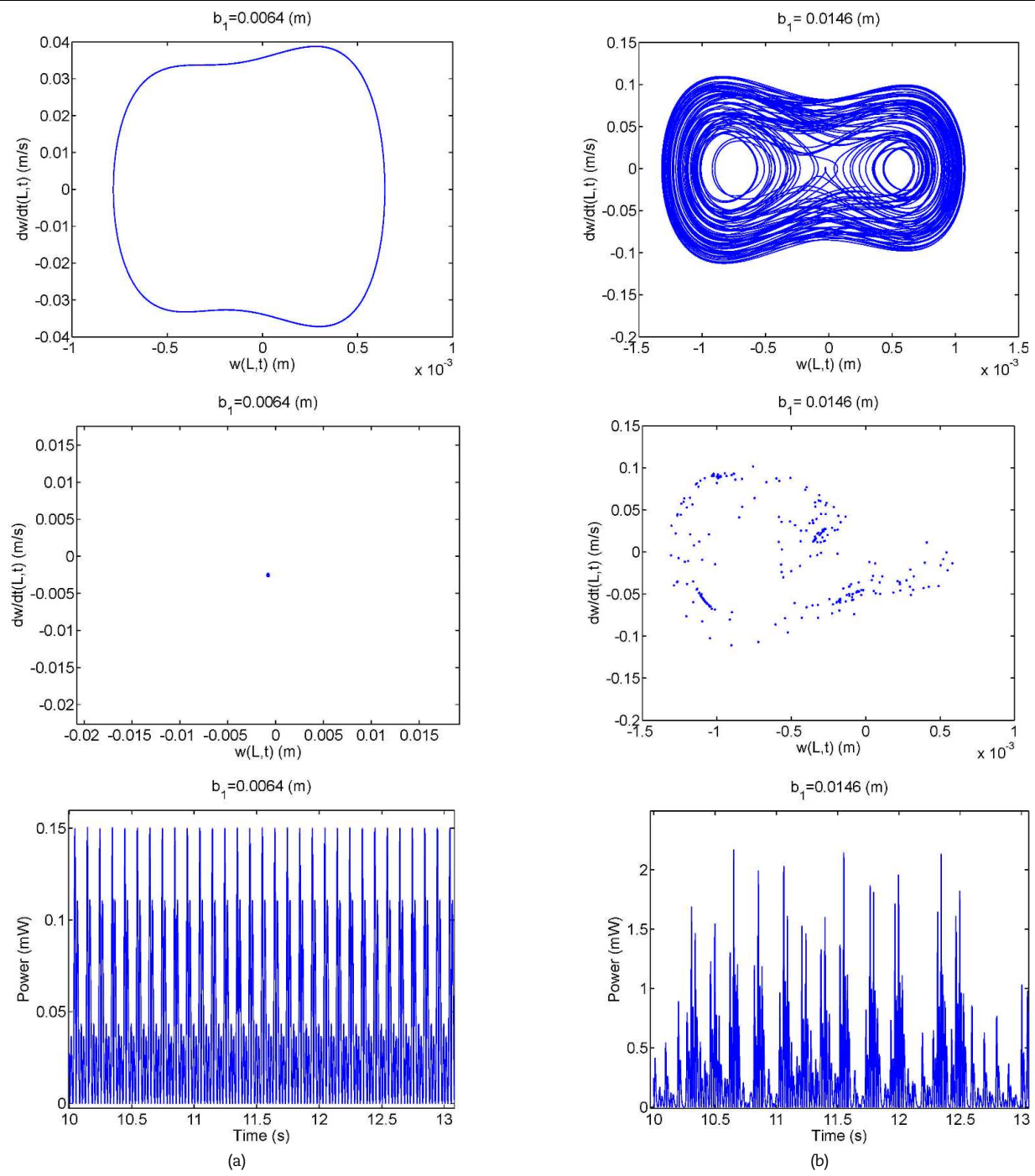


Fig. 16. Validation of bifurcation diagram by phase plane, Poincare map, and output power time series for (a) at periodic, (b) chaotic.

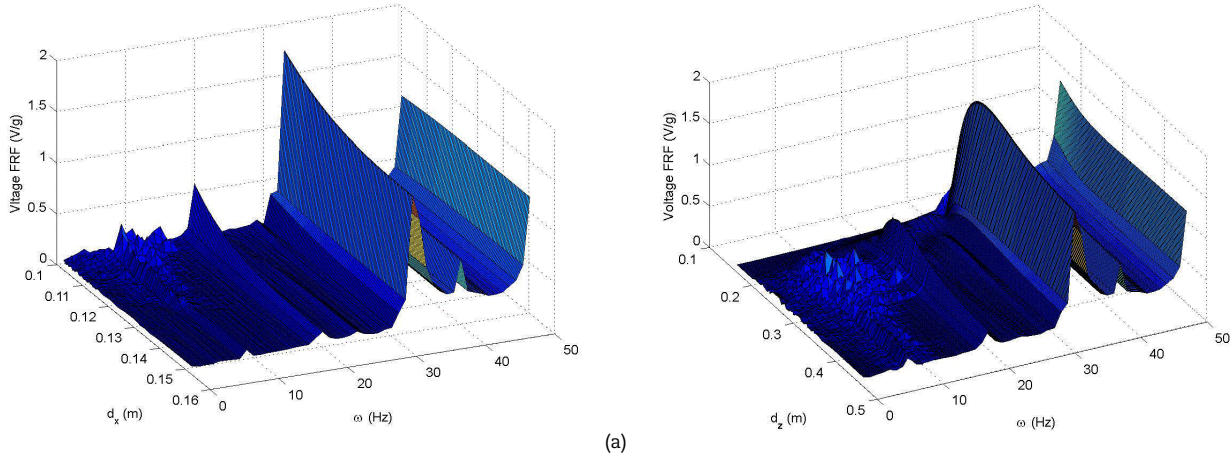
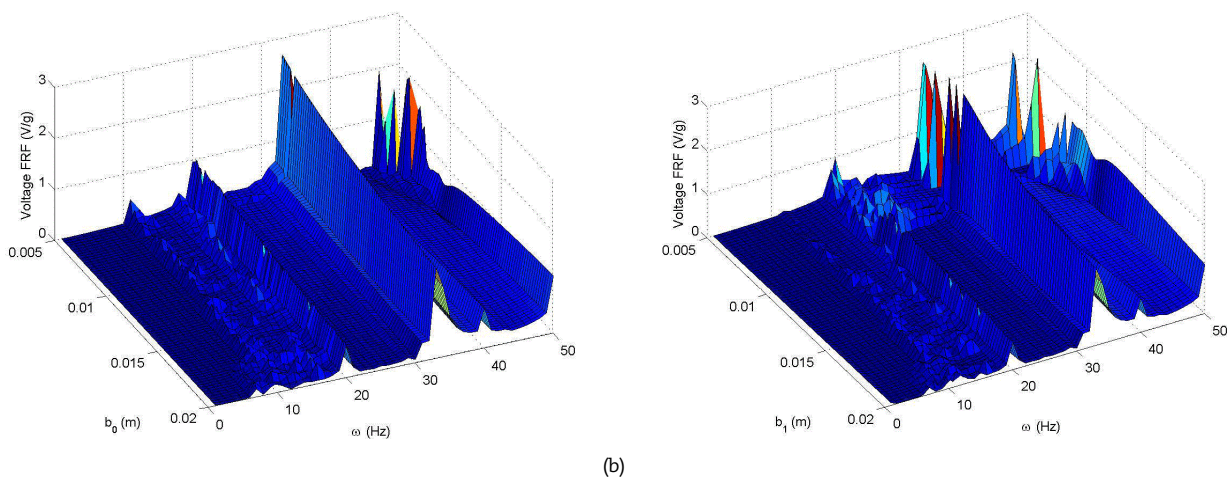


Fig. 17. Waterfall diagram: (a) Tapered beam with $b_0 = 0.02$ m, $b_1 = 0.01$ m, (b) Tapered beam with $d_x = 0.092$ m, $d_z = 0.192$ m.



**Fig. 17.** Continued.

4. Conclusions

The effect of the beam profile of a vibratory energy harvesting system on the output power and the nonlinear dynamic behavior was studied. The physical model used here comprises of the upper and lower piezoelectric layers on a trapezoidal cantilever beam with one attached tip magnet and two external magnets. The electromechanical Lagrange equations were used to derive the electrical and vibrational equations. The proposed model for the bimorph and magnetic forces was validated by previously published experimental results. The nonlinear analysis techniques, such as the bifurcation diagrams, phase plane portraits, and Poincare maps, were used to investigate the dynamic behavior of the system. The comparison of the harvested power from the rectangular and trapezoidal beam profiles was performed for various bifurcation parameters. The obtained results are summarized as follows:

- Comparison of the harvested power from the rectangular and trapezoidal (RB, TBST, and TBSR) profiles showed that the TBST profile and the RB profile had the highest and lowest power values, respectively
- In the TBST profile, the dominant behavior was periodic. Investigation of the performance of this profile showed that when the bifurcation control parameter was d_x , the maximum output power was $P_{\max} = 4.898(\text{mW})$ at $d_x = 0.0895(\text{m})$ where the dynamic behavior of the system was subharmonic (3T), and the tip deflection was slight. Also, when d_z was the bifurcation control parameter, the maximum output power was $P_{\max} = 1.886(\text{mW})$ at $d_z = 0.224(\text{m})$, where the dynamic behavior of the system was chaotic.
- In the TBSR profile, the dominant behavior was chaotic. The performance investigation of this profile showed that when the bifurcation control parameter was d_x , the maximum output power was $P_{\max} = 3.157(\text{mW})$ at $d_x = 0.0895(\text{m})$ where the dynamic behavior of the system was subharmonic (3T). Also, when d_z was the bifurcation control parameter, the maximum output power was $P_{\max} = 2.186(\text{mW})$ at $d_z = 0.242(\text{m})$, where the dynamic behavior of the system was chaotic.
- Investigation of the performance of the trapezoidal beam showed that when the width of the tip, b_0 , was used as bifurcation parameters, the dominant behavior was subharmonic, and the maximum output power was $P_{\max} = 2.284(\text{mW})$ at $b_0 = 0.0102(\text{m})$, where the dynamic behavior of the system was chaotic and when the root width, b_1 , was used as bifurcation parameters the dominant behavior was chaotic, and the maximum output power was $P_{\max} = 2.429(\text{mW})$ at $b_1 = 0.0088(\text{m})$, where the tip deflection was small.
- Simultaneous investigation of the effects of exciting frequency and bifurcation parameters on the system performance (voltage) was presented in the waterfall diagrams. These waterfalls showed that the output voltage increases by decreasing the respective parameters, and one could obtain the appropriate exciting frequency regions and parameter values to reach the optimum output power or the corresponding harvested power.

Author Contributions

Both authors developed the mathematical modeling and simulations. The manuscript was written through the contribution of both authors. The authors discussed the results, reviewed and approved the final version of the manuscript.

Acknowledgments

Not applicable.

Conflict of Interest

The authors declared no potential conflicts of interest with respect to the research, authorship and publication of this article.

Funding

The authors received no financial support for the research, authorship and publication of this article.

Data Availability Statements

The datasets generated and/or analyzed during the current study are available from the corresponding author on reasonable request.



References

- [1] Erturk, A., Electromechanical modeling of piezoelectric energy harvesters. Blacksburg, Virginia Polytechnic Institute and State University, November 20, 2009.
- [2] Roundy, S., Wright, P.K., A piezoelectric vibration based generator for wireless electronics, *Smart Materials and Structures*, 13, 2004, 1131-1144.
- [3] Dutoit, N.E., Wardle, B.L., Kim, S., Design considerations for MEMS-scale piezoelectric mechanical vibration energy harvesters, *Integrated Ferroelectrics*, 71, 2005, 121-160.
- [4] Sodano, H.A., Park, G., Inman, D.J., Estimation of electric charge output for piezoelectric energy harvesting, *Strain* 40, 2004, 49-58.
- [5] Karimi, M., Tikan, R., Ziae Rad, S., Mirdamadi, H.R., Experimental and theoretical studies on piezoelectric energy harvesting from low-frequency ambient random vibrations, *Proc. IMechE C: J Mechanical Engineering Science*, 230(14), 2015, 2363-2375.
- [6] De Marqui, C.Jr., Erturk, A., Inman, D.J., An electromechanical finite element model for piezoelectric energy harvester plates, *Journal of Sound and Vibration*, 327, 2009, 9-25.
- [7] Elvin, N.G., Elvin, A.A., A coupled finite element circuit simulation model for analyzing piezoelectric energy generators, *Journal of Intelligent Material Systems and Structures*, 20, 2009, 587-595.
- [8] Giorgio, De.P., Aurelio, S., Nicolò, Z., Design, Simulation, and Testing of Energy Harvesters With Magnetic Suspensions for the Generation of Electricity From Freight Train Vibrations, *Journal of Computational and Nonlinear Dynamics*, 7(4), 2012, 041011.
- [9] Erturk, A., Inman, D.J., Issues in mathematical modeling of piezoelectric energy harvesters, *Smart Materials and Structures*, 17, 2008, 0650016.
- [10] Erturk, A., Inman, D.J., A distributed parameter electromechanical model for cantilevered piezoelectric energy harvesters, *Journal of Vibration and Acoustics*, 130, 2008, 041002.
- [11] Erturk, A., Inman, D.J., An experimentally validated bimorph cantilever model for piezoelectric energy harvesting from base excitations, *Smart Materials and Structures*, 18, 2009, 025009.
- [12] Mann, B.P., Sims, N.D., Energy harvesting from the nonlinear oscillations of magnetic levitation, *Journal of Sound and Vibration*, 319, 2009, 515-30.
- [13] Zhao, S., Erturk, A., Electroelastic modeling and experimental validations of piezoelectric energy harvesting from broadband random vibrations of cantilevered bimorphs, *Smart Materials and Structures*, 22, 2013, 015002.
- [14] Abdelmoula, H., Zimmerman, S., Abdelkefi A., Accurate modeling, comparative analysis and performance enhancement of broadband piezoelectric energy harvesters with single and dual magnetic forces, *International Journal of Non-Linear Mechanics*, 95, 2017, 355-363.
- [15] Stanton, S.C., McGehee, C.C., Mann, B.P., Nonlinear dynamics for broadband energy harvesting: Investigation of a bistable piezoelectric inertial generator, *Journal of Physics D*, 239, 2010, 640-653.
- [16] Firoozy, P., Khadem, S.E., Pourkiaee, S.M., Broadband energy harvesting using nonlinear vibrations magnetopiezoelectric cantilever beam, *International Journal of Engineering Science*, 111, 2017, 113-133.
- [17] Aravind, K., Shaikh Faruque, A., Arockiarajan, A., Influence of Piezoelectric Energy Transfer on the Interwell Oscillations of Multistable Vibration Energy Harvesters, *Journal of Computational and Nonlinear Dynamics*, 14(3), 2019, 031001.
- [18] Cao, J., Zhou, S., Inman, D.J., Nonlinear Dynamic Characteristics of Variable Inclination Magnetically Coupled Piezoelectric Energy Harvesters, *Journal of Vibration and Acoustics*, 137, 2015, 1-9.
- [19] Noll, M.U., Lentz, L., Wagner, U., On the Improved Modeling of the Magnetoelastic Force in a Vibrational Energy Harvesting System, *Journal of Vibration Engineering & Technologies*, 2019, <https://doi.org/10.1007/s42417-019-00134-z>.
- [20] Ramian, R., Brennan, M.J., Mace, B.R., Potential benefits of a non-linear stiffness in an energy harvesting device, *Nonlinear Dynamics*, 59, 2010, 545-58.
- [21] Vijayan, K., Friswell, M.I., Haddad, K., Non-linear energy harvesting from coupled impacting beams, *International Journal of Mechanical Sciences*, 96, 2015, 101-9.
- [22] Stanton, S.C., Erturk, A., Mann, B.P., Nonlinear neoconservative behavior and modeling of piezoelectric energy harvesters including proof mass effects, *Journal of Intelligent Material Systems and Structures*, 23, 2011, 183-199.
- [23] Abdelkefi, A., Nayfeh, A.H., Hajj, M.R., Global nonlinear distributed-parameter model of parametrically excited piezoelectric energy harvesters, *Nonlinear Dynamics*, 67, 2012, 1147-1160.
- [24] Geiyer, D., Kauffman, J.L., Chaotification as a Means of Broadband Energy Harvesting with Piezoelectric Materials, *Journal of Vibration and Acoustics*, 137, 2015, 1-8.
- [25] Masana, R., Daqaq, M.F., Relative performance of a vibratory energy harvester in mono- and bi-stable potentials, *Journal of Sound and Vibration*, 330, 2011, 6036 - 6052.
- [26] Daqad, M.F., Masana, R., Erturk, A., On the Role of Nonlinearities in Vibratory Energy Harvesting: A Critical Review and Discussion, *Applied Mechanics Reviews*, 66, 2014, 1-23.
- [27] Harte, P., Blokhina, E., Feely, O., et al., Electrostatic Vibration Energy Harvesters with Linear and Nonlinear Resonators, *International Journal of Bifurcation and Chaos*, 24, 2014, 1430030-34.
- [28] Khanlo, H.M., Dehghani, R., The effect of distance and dimensions of magnets on nonlinear behavior of piezomagnetoelastic bimorph energy harvester, *Journal of Theoretical and Applied Vibration and Acoustics*, 4(1), 2018, 37-64.
- [29] Xu, M., Li, X., Stochastic averaging for bistable vibration energy harvesting system, *International Journal of Mechanical Sciences*, 141, 2018, 206-212.
- [30] Mokem Fokou, I.S., Nono Dueyou Buckjohn, C., Tchawoua, C., Probabilistic distribution and stochastic P-bifurcation of a hybrid energy harvester under colored noise, *Communications in Nonlinear Science and Numerical Simulation*, 56, 2018, 177-197.
- [31] Deng, H., Du, Y., Wang, Z., Ye, J., Zhang, J., Ma, M. & Zhong, X., Poly-stable energy harvesting based on synergistic multistable vibration, *Communications Physics*, 2(21), 2019. <https://doi.org/10.1038/s42005-019-0117-9>.
- [32] Litak, G., Abadal, G., Rysak, A., Przywara, H., Complex dynamics of a bistable electrically charged microcantilever: Transition from single well to cross well oscillations, *Chaos, Solitons & Fractals*, 99, 2017, 85-90.
- [33] Benasciutti, D., Moro, L., Zelenika, S., Brusa, E., Vibration energy scavenging via piezoelectric bimorphs of optimized shapes, *Microsystem Technologies*, 16, 2010, 657-668.
- [34] Ben Ayed, S., Abdelkefi, A., Naja, F.R., Hajj, M., Design and performance of variable-shaped piezoelectric energy harvesters, *Journal of Intelligent Material Systems and Structures*, 25, 2014, 174-186.
- [35] Biswal, A.R., Roy, T., Behera, R.K., Genetic algorithm-and finite element-based design and analysis of nonprismatic piezolaminated beam for optimal vibration energy harvesting, *Proc. IMechE C: J Mechanical Engineering Science*, 230(14), 2015, 2532-2548.
- [36] Xie, X.D., Carpenteri, A., Wang, Q., A theoretical model for a piezoelectric energy harvester with a tapered shape, *Engineering Structures*, 144, 2017, 19-25.
- [37] Erturk, A., Inman, D.J., *Piezoelectric Energy Harvesting*, Ltd. Publication, John Wiley and Sons, 2011.
- [38] Griffiths, D.J., *Introduction to Electrodynamics*, 4th ed. Ltd., Publication, Prentice Hall, 2013.
- [39] Kim, P., Seok, J., A multi stable energy harvester: Dynamic modeling and bifurcation analysis, *Journal of Sound and Vibration*, 333, 2014, 5525-5547.
- [40] Yong, K., Landecker, P., Villani, D., An analytic solution for the force between two magnetic dipoles, *Magnetic and Electrical Separation*, 9, 1998, 39-52.
- [41] Nayfeh, A.H., Pai, P.F., *Linear and Nonlinear Structural Mechanics*, Wiley Series in Nonlinear Science. Wiley, New York, 2004.
- [42] Stanton, S.C., Erturk, A., Mann, B.P., Inman, D.J., Nonlinear piezoelectricity in electroelastic energy harvesters: Modeling and experimental identification, *Journal of Applied Physics*, 108, 2010, 074903-9.

Appendix A: Matrices utilized in equations of motion (28)

At first, the following matrices are defined.

$$\begin{aligned}
 M_{ij}^k &= 4 \int_{V_k} \rho_k \sum_{r,p=1}^n R_{ip} R_{jr} q_r q_p dV_k - 4 \int_{V_k} \rho_k \sum_{r=1}^n R_{ir} \psi'_r q_r z dV_k + \int_{V_k} \rho_k \psi'_i \psi'_j z^2 dV_k + \int_{V_k} \rho_k \psi_i \psi_j dV_k \\
 H_i^k &= \int_{V_k} \rho_k \psi_i(x) dV_k
 \end{aligned} \tag{A.1}$$



where $k = s, p_1, p_2$ denotes structure, upper and lower piezoelectric layers, respectively. Also, the following relations are defined for the tip magnet.

$$\begin{aligned} M_{ij}^L &= 4M \sum_{r,p=1}^n R_{ip}(L)R_{jr}(L)q_r q_p - M\psi_i(L)\psi_j(L) + I_M\psi_i'(L)\psi_j'(L) \\ H_i^L &= M\psi_i(L) \end{aligned} \quad (\text{A.2})$$

Also, the following relations are considered.

$$\begin{aligned} K_{ij}^\sigma &= \frac{1}{4} \int_{V_\sigma} E_\sigma \sum_{r,p=1}^n \psi_r' \psi_p' \psi_i' \psi_j' q_r q_p dV_\sigma + \int_{V_\sigma} E_\sigma z^2 \psi_i''(x) \psi_j''(x) dV_\sigma \\ &\quad + \int_{V_\sigma} E_\sigma z \sum_{r=1}^n \psi_r' \psi_i' \psi_j' q_r dV_\sigma \quad \& \quad \sigma = s, p_1, p_2 \\ G_i^\sigma &= \frac{1}{2} \int_{V_\sigma} e_{31} \sum_{j=1}^n \psi_i' \psi_j' q_j dV_\sigma + \int_{V_\sigma} e_{31} z \psi_i' dV_\sigma \quad \& \quad \sigma = p_1, p_2 \end{aligned} \quad (\text{A.3})$$

Now, the elements of matrices \mathbf{M} , \mathbf{K} , \mathbf{H} and \mathbf{G} used in (28) are obtained as follows:

$$\begin{aligned} M_{ij} &= M_{ij}^s + M_{ij}^{p_1} + M_{ij}^{p_2} + M_{ij}^L \\ K_{ij} &= K_{ij}^s + K_{ij}^{p_1} + K_{ij}^{p_2} \\ H_i &= H_i^s + H_i^{p_1} + H_i^{p_2} \\ G_i &= G_i^{p_1} + G_i^{p_2} \end{aligned} \quad (\text{A.4})$$

ORCID iD

Heshmatallah Mohammad Khanlo  <https://orcid.org/0000-0002-7913-3820>
Reza Dehghani  <https://orcid.org/0000-0002-5268-0402>



© 2022 Shahid Chamran University of Ahvaz, Ahvaz, Iran. This article is an open access article distributed under the terms and conditions of the Creative Commons Attribution-NonCommercial 4.0 International (CC BY-NC 4.0 license) (<http://creativecommons.org/licenses/by-nc/4.0/>).

How to cite this article: Mohammad Khanlo H., Dehghani R. Distributed-parameter Dynamic Modeling and Bifurcation Analysis of a Trapezoidal Piezomagnetoelastic Energy Harvester, *J. Appl. Comput. Mech.*, 8(1), 2022, 97–113.
<https://doi.org/10.22055/JACM.2019.30823.1785>

Publisher's Note Shahid Chamran University of Ahvaz remains neutral with regard to jurisdictional claims in published maps and institutional affiliations.

